Atomic Spectroscopy

Article

Machine Learning-assisted Multimodal Spectroscopy for Rapid Quantification of NiO/YSZ and Ni/YSZ Anode Composition

Shaobo Feng, Weiran Song, Minfang Han,* and Zhe Wang*

State Key Laboratory of Power System Operation and Control, Department of Energy and Power Engineering, Tsinghua University, Beijing 100084, P. R. China

Received: *July 31, 2026;* ***Revised:*** *September20, 2026;* ***Accepted:*** *October 05, 2026;* ***Available online:*** *October 05, 2026.*

DOI: 10.46770/AS.2026.0071s

ABSTRACT: Conventional techniques such as X-ray diffraction and scanning electron microscopy coupled with energy-dispersive X-ray spectroscopy are commonly employed for solid oxide fuel cell (SOFC) anode characterisation to provide information on phase composition and local elemental distribution. However, these methods generally involve limited measurement coverage, relatively high analytical costs, and complex operating procedures, restricting their application to the rapid evaluation of large-area SOFC anode samples. In this work, laser-induced breakdown spectroscopy (LIBS), hyperspectral imaging (HSI), and smartphone video imaging (SVI), combined with machine learning, were applied to rapidly quantify the nominal NiO mass fraction in sintered NiO/YSZ and corresponding reduced Ni/YSZ samples. Specifically, LIBS acquired atomic emission spectra that reflected elemental information of Ni and Zr, whereas HSI and SVI recorded reflectance signals and RGB colour responses, respectively. Four regression algorithms, including partial least squares regression, locally weighted partial least squares regression, kernel extreme learning machine, and support vector regression, were employed to establish relationships between the acquired signals and nominal NiO mass fraction. LIBS exhibited the best single-modality performance, with maximum R^2 values of 0.9854 and 0.9860 for the sintered and reduced samples, respectively. Further, decision-level LIBS-SVI and HSI-SVI fusion were investigated. Adding SVI improved predictive performance in most model-modality combinations, with lower RMSE values obtained in 14 of the 16 evaluated fusion cases compared with the corresponding LIBS- or HSI-based single-modality models. Overall, SVI provided useful complementary information while introducing little additional equipment cost or measurement complexity.

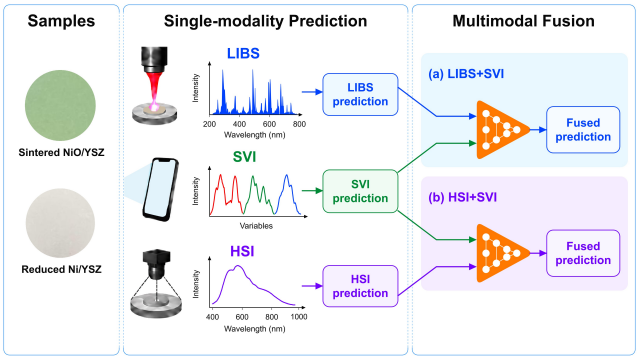

INTRODUCTION

Solid oxide fuel cells (SOFCs) are efficient electrochemical devices that directly convert the chemical energy of fuels into electricity. Owing to their high conversion efficiency, fuel flexibility and relatively low pollutant emissions, SOFCs have considerable potential for stationary power generation, distributed energy systems and combined heat and power applications.[1] A typical SOFC is composed of an anode, an electrolyte and a cathode, among which the anode plays a critical role in fuel oxidation, electron conduction and gas transport. Nickel-yttria-stabilized zirconia (Ni/YSZ) cermets are among the most widely used SOFC anode materials. Metallic Ni provides high electronic conductivity and catalytic activity, and YSZ offers ionic conductivity, structural support and compatibility with the electrolyte.[2] The relative contents and distributions of Ni and YSZ affect the continuity of electronic and ionic transport networks, gas accessibility and the distribution of electrochemically active triple-phase boundaries (TPBs), which may affect electrochemical performance and long-term stability.[3,4] During actual cell operation, various factors, such as redox cycling and Ni migration, can affect the relative content and distribution of Ni and YSZ.[5,6]

NiO/YSZ composites are commonly used to manufacture Ni/YSZ anodes. During fabrication, NiO and YSZ powders are mixed, pressed and sintered to obtain a mechanically stable composite structure. The sintered NiO/YSZ material is subsequently reduced in a hydrogen atmosphere, during which

NiO is converted into metallic Ni and a porous Ni/YSZ anode is formed.[7] Therefore, variations in the relative content of NiO and YSZ in the precursor can directly affect the final Ni/YSZ composition and structure after reduction.[4] Quantitative determination of the Ni-based component in both sintered NiO/YSZ and reduced Ni/YSZ materials is therefore important for identifying composition deviations during preparation and quality control. Conventional methods such as X-ray diffraction (XRD), scanning electron microscopy (SEM) coupled with energy-dispersive X-ray spectroscopy (EDS) and X-ray fluorescence spectroscopy (XRF) can provide phase, local elemental or bulk-composition information.[8] However, their relatively high analytical costs, limited measurement coverage, and potentially complex operating procedures restrict their application to the rapid analysis of large-area anode samples. Therefore, analytical techniques with lower costs, broader measurement coverage and simpler operation are desirable for the rapid, high-throughput analysis of large-area anode samples.

Quantification of NiO/YSZ and Ni/YSZ anode composition is fundamentally an elemental composition problem, because the relative abundance of the Ni component can be characterised by the elemental responses of Ni and Zr. Laser-induced breakdown spectroscopy (LIBS) uses a focused laser pulse to ablate a minute amount of material from the sample surface and generate a transient plasma. During plasma cooling, excited atoms and ions emit characteristic spectral lines, which can be used for elemental identification and quantification.[9,10] Owing to its direct sensitivity to elemental composition, LIBS is therefore suitable for this quantitative analysis task. The technique enables rapid and simultaneous multi-element analysis with minimal sample preparation. Its feasibility for electrode materials has already been demonstrated in lithium-ion batteries. Imashuku et al. used LIBS to quantitatively map Li in $LiCoO_2$ cathodes, obtaining Li distributions consistent with those measured by X-ray absorption spectroscopy.[11] Smyrek et al. demonstrated that LIBS enables the quantitative determination of Li concentration profiles in both structured and unstructured NMC electrodes.[12] Kappeler et al. used LIBS signals of Li, Ni, Mn, Co and other elements to assess cathode-coating homogeneity and identify manufacturing irregularities.[13] These results demonstrate that LIBS can resolve elemental composition in complex electrode matrices. Moreover, recent advances in machine learning-assisted LIBS analysis have shown that data-driven models can effectively capture nonlinear relationships between spectral features and target compositions, further improving quantitative analysis performance in complex systems.[14] The characteristic emission lines of Ni and Zr in LIBS spectra can provide element-specific descriptors related to SOFC anode composition, indicating the feasibility of LIBS for rapid quantitative analysis. However, its application to the compositional analysis of SOFC anode materials has not been widely investigated.

In SOFC anode samples, variations in the relative content of Ni and YSZ are associated with changes in the surface morphology and porosity of Ni/YSZ anodes.[15] Such compositional and microstructural variations may also influence the surface optical response, including colour and wavelength-dependent reflectance. Hyperspectral imaging (HSI) and smartphone video imaging (SVI) can both rapidly acquire high-dimensional optical responses and are thus capable of distinguishing the optical changes caused by differences in composition. HSI records a continuous reflectance spectrum at each pixel to form a three-dimensional data cube, enabling non-destructive prediction and compositional mapping.[16] In a directly relevant reflectance study, Richter et al. applied visible-to-infrared spectroscopy and HSI to distinguish Al, Cu and residual fractions in shredded lithium-ion battery materials, identifying 400-1000 nm as an effective range for material discrimination.[17] Chouhan et al. combined HSI with convolutional-autoencoder-based spectral unmixing to detect and distinguish Cu and Al foils in shredded lithium-ion battery materials, demonstrating its capability for spatially resolved identification of battery components.[18] SVI records short videos of samples under sequential illumination generated by a colour-changing smartphone screen. The acquired video frames are then decomposed into RGB channels to construct a high-dimensional signal containing spatial and illumination-dependent optical information.[19] Compared with HSI, SVI requires no dedicated spectrometer and offers lower cost, greater accessibility and reduced operational complexity. Smartphone-video studies have achieved quantitative adulteration prediction with R^2 of 0.98 and have further demonstrated classification of heterogeneous samples, component-distribution mapping and hyperspectral image reconstruction.[19,20] Thus, HSI and SVI can potentially capture composition-related optical differences in NiO/YSZ and Ni/YSZ materials, providing rapid and non-destructive approaches for SOFC anode quantification and spatial assessment.

LIBS, HSI and SVI exhibit complementary measurement mechanisms. LIBS provides direct element-specific information through characteristic plasma emission lines. HSI records spatially resolved and wavelength-dependent reflectance spectra under controlled illumination. SVI captures dynamic RGB responses under sequentially varied colour illumination. Yao et al. demonstrated the value of combining LIBS with HSI, as the elemental information provided by LIBS can be complemented by the spatial and surface optical information obtained from HSI.[21] Such integration can compensate for signal uncertainty and improve quantitative analysis or material-identification performance. In a representative study, Zhao et al. integrated sparse LIBS measurements with HSI data to reconstruct elemental-distribution images, substantially improving spatial resolution while reducing scanning time compared with conventional LIBS imaging.[22] However, LIBS-HSI systems require both a LIBS instrument and a dedicated hyperspectral camera, resulting in increased equipment cost and measurement

complexity. LIBS-SVI fusion offers a more economical alternative by supplementing direct elemental signals with RGB responses acquired using a smartphone, without substantially increasing hardware cost or operational complexity. SVI and HSI may also provide complementary optical information because HSI measures detailed wavelength-resolved reflectance, whereas SVI records dynamic surface responses under actively varied colour illumination. Their integration may therefore combine the high spectral resolution of HSI with the low cost, accessibility and flexible illumination strategy of SVI. For SOFC anodes, LIBS-SVI and HSI-SVI fusion may capture complementary elemental, reflectance and colour-response variations, providing practical and cost-effective strategies for improving the accuracy and robustness of NiO/YSZ and Ni/YSZ composition quantification.

In this study, LIBS, HSI and SVI were combined with machine-learning algorithms to quantify the nominal NiO mass fraction in sintered NiO/YSZ samples and reduced Ni/YSZ samples. The predictive performance of several commonly employed regression methods was first evaluated separately for each modality to establish reliable single-modality models. Decision-level data fusion was subsequently performed through two pairwise fusion schemes, namely LIBS-SVI and HSI-SVI, to improve composition prediction. Specifically, independent models were developed and optimised for each modality, after which their prediction outputs were combined through a weighted fusion strategy, allowing each technique to contribute according to its predictive reliability. This study investigates the feasibility of integrating element-specific atomic emission spectra and spectroscopic information based on reflectance for rapid composition analysis. Moreover, incorporating SVI into LIBS- and HSI-based analysis introduces complementary RGB information without substantially increasing equipment cost or measurement complexity. This study therefore evaluates the feasibility of multimodal spectroscopy for rapid and cost-effective SOFC anode composition analysis.

EXPERIMENTAL

Sample preparation. NiO powder and 8 mol% yttria-stabilized zirconia (8Y-YSZ) powder were used to prepare model SOFC anode materials with nominal NiO mass fractions ranging from 0 to 100 wt%. Composition intervals of 5 wt% were adopted in the ranges of 0-35 wt% and 65-100 wt%, and an interval of 2 wt% was used between 35 and 65 wt%, with an additional composition level at 50 wt%. In total, 31 composition levels were prepared, with four independently fabricated pellets at each level, yielding 124 samples. For each composition, NiO and 8Y-YSZ powders were weighed according to the designed mass ratio to obtain 20 g of mixed powder, after which 0.3 g of polyvinyl butyral (PVB) was added as a binder. Acetone was introduced as the grinding and dispersion medium, and the mixture was ground for approximately 1.5 h until the solvent had completely evaporated, producing a fine and visually homogeneous powder. Subsequently, 3.0 g of the processed powder was loaded into a circular die and pressed at 15 MPa for 3 min to form pellets with a diameter of 30 mm. The green pellets were placed on alumina supports and sintered in a muffle furnace using a multistep heating programme. The temperature was increased to 600 °C at 2 °C min^{-1} and held for 1 h to remove the organic binder, then raised to 1000 °C at 2 °C min^{-1} and held for 1 h, followed by heating to 1350 °C at 1 °C min^{-1} and holding for 5 h. The pellets were subsequently cooled to room temperature to obtain the sintered NiO/YSZ samples.

Two pellets of each composition level were reduced in a tubular furnace to obtain the corresponding Ni/YSZ samples. Before heating, the furnace tube was purged with nitrogen to remove residual air. The samples were then heated to 750 °C and reduced in a hydrogen atmosphere for 3 h, during which NiO was converted into metallic Ni and a porous Ni/YSZ structure was formed. After reduction, the samples were cooled to room temperature under nitrogen protection to minimise reoxidation. The reduced samples retained the composition labels defined by the initial NiO mass fractions in the precursor mixtures, thereby maintaining a one-to-one correspondence with the sintered samples. Accordingly, the composition values used in subsequent modelling refer to the nominal NiO mass fraction before reduction rather than the actual metallic Ni mass fraction after reduction. Two matched sample sets were therefore obtained: 62 sintered NiO/YSZ samples and 62 corresponding reduced Ni/YSZ samples. Fig. 1 presents the appearance of sintered NiO/YSZ samples and reduced Ni/YSZ samples. For the sintered samples, the colour gradually changed from light green to darker green as the NiO content increased from 10% to 90%, indicating that the surface optical characteristics were related to the sample composition. After reduction, the colour difference became less obvious.

SVI, HSI and LIBS measurements. For each material state, the non-destructive optical measurements were performed before LIBS acquisition. The sintered NiO/YSZ samples were first measured by SVI and HSI, followed by LIBS. The same measurement sequence was repeated after the samples had been reduced to Ni/YSZ. During all measurements, the acquisition parameters and sample positions were kept consistent and all the measurements were completed within the same period to reduce variations caused by instrumental and environmental conditions. The LIBS, SVI and HSI measurements generated three complementary types of data. LIBS offered element-specific information, HSI supplied reflectance information at different wavelengths, and SVI provided RGB channel responses.

For LIBS measurements, a benchtop LIBS system (ChemReveal LIBS Desktop Elemental Analyzer 3766, TSI Inc.,

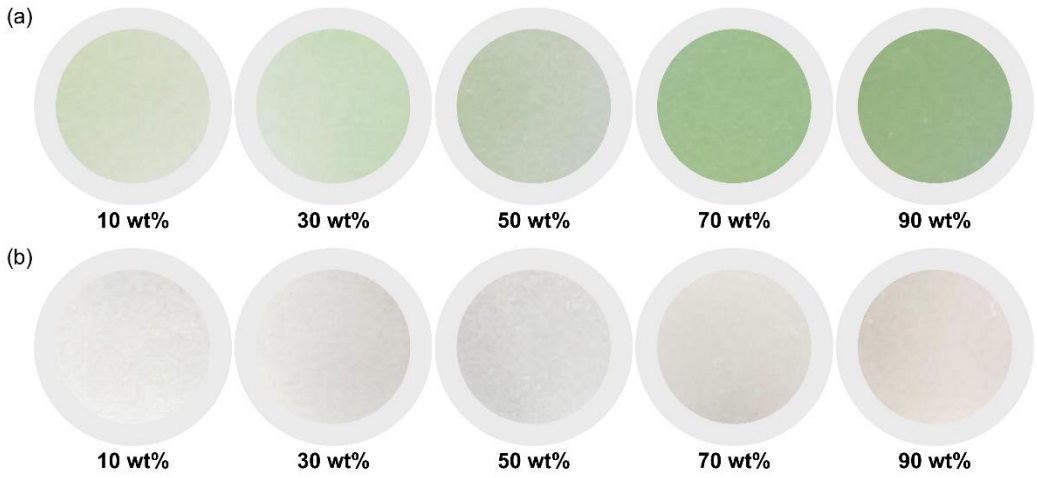

Fig. 1 Appearance of sintered NiO/YSZ samples and reduced Ni/YSZ samples. (a) Sintered NiO/YSZ samples, (b) Reduced Ni/YSZ samples.

Shoreview, MN, USA) consisting of a Q-switched Nd:YAG laser and a seven-channel CCD spectrometer was employed. During measurement, the pulsed laser was focused onto the sample surface, causing local ablation and generating a transient plasma. The plasma-emission signal was collected to form the spectra on the computer. Each sample was measured using a 10 × 10 point grid, yielding 100 LIBS spectra distributed over the central surface region. The laser spot diameter was 100 μm, and the spacing between adjacent sampling points was 800 μm. The laser-pulse energy was set to 38 mJ, and the acquisition frequency was 2 Hz. Each raw LIBS spectrum contained 12,990 wavelength variables and covered a spectral range from 186.9 nm to 979.2 nm with a resolution of 0.09 nm.

HSI data were acquired using a visible near-infrared HSI system consisting of two light sources (3900, Illumination Technologies Inc., USA), an imaging spectrograph (Imspector V10E, Specim Ltd., Finland), a camera (Falcon EM285CL, Raptor Photonics Led., UK), a translation stage and data-acquisition software. The samples were placed on the motorised stage and scanned line by line under stable illumination. The exposure time was fixed at 21.231 ms per line, the camera frame rate was set to 33 fps, and the translation speed was set to approximately 1.4 mm s^{-1}. The acquired hyperspectral data contained 616 spectral bands, with a spectral range from 342-1002 nm and 1 nm spectral resolution. The acquisition conditions were kept unchanged for all sintered and reduced samples to ensure comparability between measurements.

For SVI acquisition, a Samsung Galaxy S21+ 5G smartphone equipped with a special SVI application was fixed relative to the sample. The smartphone screen served as the active illumination source and sequentially displayed a preset series of gradually changing colours by adjusting the relative proportions of the RGB channels, while the front-facing camera recorded the reflected colour responses from the sample surface.[23] The smartphone screen brightness was fixed at the maximum level, and the application used an HSV colour sequence containing 1000 programmed colour steps. To minimise interference from ambient light, the measurements were conducted in a dark chamber, with the smartphone positioned parallel to the sample surface at a fixed working distance of approximately 10 cm. Before each recording, automatic exposure and automatic white balance were locked, while autofocus remained in automatic mode. ISO was not manually assigned but was determined by the automatic exposure setting before exposure was locked. Each video was recorded at 30 fps with a resolution of 1080 × 1920 pixels and a duration of approximately 6 s. The fixed sample holder, imaging distance, illumination sequence, camera settings, and acquisition environment ensured that differences in the recorded video signals were primarily associated with the optical responses of the samples.

METHODOLOGY

Data preprocessing. The LIBS, SVI and HSI measurements provide spectral information based on different physical mechanisms. Therefore, different preprocessing strategies were applied to each modality according to the characteristics of the signals. For LIBS data, the spectral lines associated with Ni and Zr were first identified with reference to the National Institute of Standards and Technology (NIST) Atomic Spectra Database to obtain characteristic peaks, followed by baseline subtraction, peak area calculation and standard normal variate (SNV) normalisation. These procedures retained element-related spectral features while reducing baseline and intensity variations. 227 peak-area variables for NiO samples and 231 peak-area variables for Ni samples were

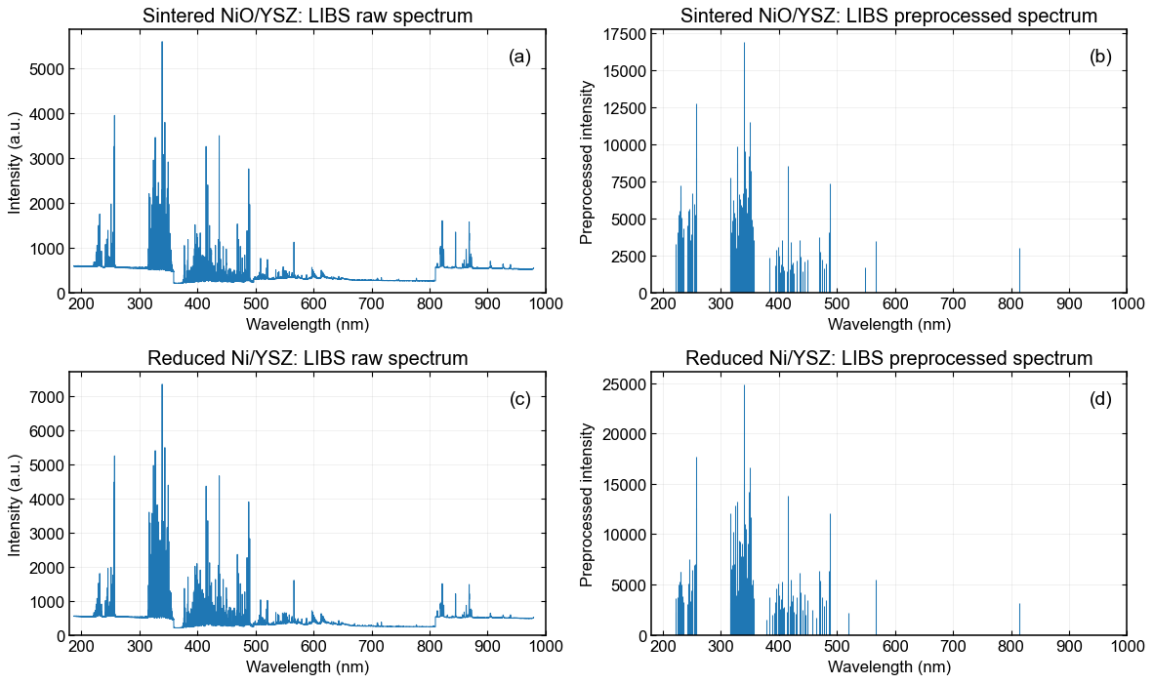

Fig. 2 Raw and preprocessed LIBS spectra of representative SOFC anode samples before SNV: (a) raw spectrum of sintered NiO/YSZ, (b) preprocessed spectrum of sintered NiO/YSZ, (c) raw spectrum of reduced Ni/YSZ, and (d) preprocessed spectrum of reduced Ni/YSZ.

subsequently extracted for quantitative modelling. By averaging information from multiple sampling points, the influence of local heterogeneity and shot-to-shot fluctuations was reduced. For HSI data, white and dark reference spectra were first obtained. The mean spectrum extracted from a 200×200 pixel ROI was then corrected using $R = (I - D)/(W - D)$, where I, D and W represent the sample, dark reference, and white reference signals, respectively. The corrected reflectance spectra were subsequently used for modelling. For SVI data, the acquired video was divided into 184 consecutive frames. A region of 180×180 pixels was selected as the region of interest (ROI) in each frame. The red, green and blue channel responses were extracted and concatenated in sequence, producing a 552-variable SVI signal for each spatial pixel. The averaged ROI signal was normalised to 0-1. After preprocessing, three independent feature matrices were obtained for LIBS, HSI and SVI. These datasets were subsequently used for single-modality quantitative prediction and multimodal fusion analysis.

Figure 2 shows the raw and preprocessed LIBS spectra of representative sintered NiO/YSZ and reduced Ni/YSZ samples. The raw spectra of the sintered and reduced samples are presented in Fig. 2 (a) and (c), respectively, and contain numerous emission peaks distributed over a broad wavelength range together with continuous background signals. After preprocessing without SNV, the noninformative wavelength regions and baseline variations were largely removed, while the composition-related spectral features were retained, as shown in Fig. 2 (b) and (d). The sintered and reduced samples exhibit similar major peak positions, indicating the presence of common constituent elements, whereas differences in their relative peak intensities reflect changes in elemental response and sample state after reduction. The processed spectra therefore provide more compact and informative inputs for subsequent quantitative modelling.

Figure 3 demonstrates mean HSI and SVI responses of representative sintered NiO/YSZ and reduced Ni/YSZ samples before normalisation. As shown in Fig. 3 (a) and (b), the HSI spectra exhibit broad wavelength-dependent variations across 342-1002 nm. Although the sintered and reduced samples show generally similar spectral profiles, differences in peak intensity and curve shape indicate that the reduction process alters their optical intensity characteristics. Fig. 3 (c) and (d) present the SVI signals formed by sequentially concatenating the R, G and B channel responses. Distinct intensity variations are observed within the three channel regions, and the response patterns differ between the sintered and reduced samples. These results indicate that HSI and SVI capture complementary wavelength-resolved reflectance and dynamic colour response information, respectively, providing informative inputs for subsequent quantitative modelling.

Single-modality quantitative prediction. To evaluate the quantitative prediction capability of each modality, independent

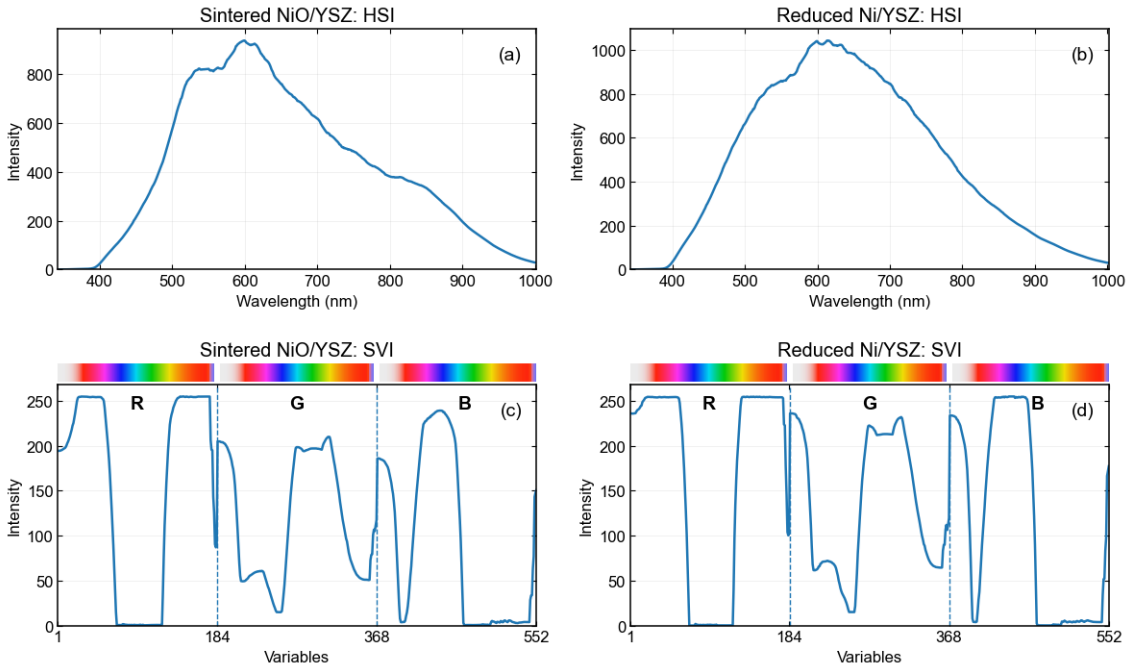

Fig. 3 Mean HSI and SVI responses of representative SOFC anode samples before normalisation: (a) HSI spectrum of sintered NiO/YSZ, (b) HSI spectrum of reduced Ni/YSZ, (c) concatenated R, G and B channel responses of sintered NiO/YSZ obtained by SVI, and (d) concatenated R, G and B channel responses of reduced Ni/YSZ obtained by SVI.

regression models were established separately using the LIBS, HSI and SVI datasets. The nominal NiO mass fraction in the precursor mixture was adopted as the prediction target for both the sintered NiO/YSZ and reduced Ni/YSZ samples, enabling direct comparison of model performance before and after reduction on a consistent composition scale. Four regression algorithms were investigated: partial least squares regression (PLSR), locally weighted partial least squares regression (LW-PLSR), kernel extreme learning machine (K-ELM) and support vector regression (SVR). PLSR extracts latent variables that maximise the covariance between predictors and responses to establish a linear regression model.[24] LW-PLSR constructs a local PLSR model for each query sample by weighting calibration samples according to their similarity to that sample.[25] K-ELM employs a kernel function to construct the feature mapping and analytically determines the output weights, enabling efficient nonlinear regression without tuning hidden-layer parameters.[26] SVR constructs a regression function by minimising model complexity while allowing prediction errors within an ε-insensitive tolerance range.[27] PLSR and LW-PLSR were employed as representative linear modelling approaches, whereas K-ELM and SVR were selected to evaluate nonlinear relationships between the multimodal spectral responses and sample composition.

For the sintered NiO/YSZ dataset, all 62 samples were included in the modelling procedure. The 0 and 100 wt% compositions were retained in every training set, while the remaining nominal NiO compositions were distributed across five external folds. All replicate pellets at the same nominal NiO mass fraction were assigned to the same fold and therefore entered either the training set or the test set together. For the reduced Ni/YSZ dataset, the two samples corresponding to the 100 wt% nominal NiO mass fraction were excluded because severe morphological deformation after reduction prevented reliable spectral acquisition. The 0 wt% composition remained fixed in the training set, while the 95 wt% composition participated in the grouped cross-validation. Within each outer training set, model parameters were selected by an inner five-fold cross-validation using the same composition grouping rule. The fixed endpoint compositions retained in each outer training set were also retained in all corresponding inner-training subsets. Consequently, no nominal NiO mass fraction represented in a validation or test subset was present in the corresponding training subset. Predictive performance was assessed using root mean square error (RMSE), mean absolute error (MAE) and coefficient of determination (R^2). The mean results across the five outer validation folds were used to compare the regression algorithms and sensing modalities. The prediction outputs of the single-modality models were subsequently used for multimodal fusion.

Variable importance analysis. A PLSR-based variable importance in projection (VIP) analysis was performed for LIBS, HSI and SVI in both material states. VIP summarises the contribution of each variable to the PLS latent variables used for

composition prediction, and variables with VIP values greater than 1 were treated as influential.[24] Within each outer fold, the number of PLS latent variables was selected by composition-grouped inner cross-validation using only the outer training samples. The PLSR model was then refitted to the complete outer training set and used to calculate VIP values. The held-out samples did not participate in parameter selection or VIP estimation.

Decision-level multimodal fusion strategy. Although individual sensing modalities provide valuable composition-related information, their prediction performance may be limited by specific modality factors. Therefore, combining the prediction outputs from different modalities can exploit their complementary advantages and improve quantitative prediction performance. In this study, a decision-level fusion strategy was developed. Independent models were first established for each sensing modality, and their prediction results were subsequently combined. This strategy avoids the dimensional imbalance among different modalities and allows each sensing technique to retain its optimised modelling procedure. The general decision-level fusion model can be expressed as:

$$\hat{y}_{fusion} = w_1\hat{y}_1 + w_2\hat{y}_2 \quad (1)$$

where w_1 and w_2 represent the contribution weights of different modalities, $\hat{y}_1$ and $\hat{y}_2$ represent the predicted value from different modalities.

In this study, weighted fusion was performed by assigning a dominant contribution to the modality with higher single-modality prediction capability and using the other modality as complementary information. For LIBS-SVI fusion, LIBS was selected as the primary modality because of its elemental specificity, while SVI was introduced as an auxiliary modality:

$$\hat{y}_{fusion} = (1 - \alpha_{SVI})\hat{y}_{LIBS} + \alpha_{SVI}\hat{y}_{SVI} \quad (2)$$

where α_{SVI} represents the contribution of SVI. The value of α_{SVI} was searched within the range of 0-0.30 with an interval of 0.02, ensuring that LIBS maintained the dominant contribution.

For HSI-SVI fusion, HSI was selected as the primary modality, and SVI was introduced as an auxiliary modality:

$$\hat{y}_{fusion} = (1 - \alpha_{SVI})\hat{y}_{HSI} + \alpha_{SVI}\hat{y}_{SVI} \quad (3)$$

The optimal fusion weight was determined using internal five-fold cross-validation on the training samples:

$$\alpha^* = arg\min_{\alpha} R\,MSE(y_{train}, (1-\alpha)y_{main} + \alpha y_{aux}) \quad (4)$$

where y_{main} and y_{aux} represent the predictions from the primary and auxiliary modalities, respectively.

To avoid unnecessary degradation caused by weak complementary information,[28] a minimum improvement criterion was introduced. The fusion model was accepted only when the internal cross-validation RMSE decreased by at least 1% compared with the primary single-modality model. Otherwise, the fusion result was considered ineffective and the prediction was retained as the original single-modal prediction. This criterion reduced the risk that an auxiliary modality with weak complementary information would degrade the fused prediction performance.

The Wilcoxon signed-rank test was performed on composition-level paired absolute errors to evaluate whether the fusion models significantly improved prediction performance compared with the corresponding single-modality models. Specifically, replicate samples with the same nominal composition were first averaged to obtain one representative absolute error for each composition group. The paired Wilcoxon signed-rank test was then applied to these composition-level errors. When the fusion model showed a lower mean absolute error and the corresponding p-value was less than 0.05, the improvement of the fusion model over the single-modality model was considered statistically significant. The same fusion procedure was applied to LIBS-SVI and HSI-SVI combinations for both sintered NiO/YSZ and reduced Ni/YSZ samples.

RESULTS AND DISCUSSION

Quantitative prediction of sintered NiO/YSZ samples. To investigate the feasibility of LIBS, HSI and SVI for quantitative composition analysis of SOFC electrode materials, prediction models based on machine learning were first established using the sintered NiO/YSZ samples. Table 1 summarises the performance results of models based on different modalities across five outer validation folds. The values are presented in the form of mean (standard deviation), where the mean value and standard deviation were calculated across the five outer validation folds. Across all modality and algorithm combinations, R^2 ranged from 0.8904 to 0.9854, while RMSE and MAE ranged from 0.0244 to 0.0692 and from 0.0204 to 0.0539, respectively. LIBS achieved the best overall performance, with R^2 values of 0.9796-0.9854. In particular, the LIBs-based LW-PLSR model yielded the highest R^2 of 0.9854, together with the lowest RMSE and MAE of 0.0244 and 0.0204, respectively. HSI also showed strong predictive capability, and its K-ELM model achieved an R^2 of 0.9750, an RMSE of 0.0336 and an MAE of 0.0283. Although SVI exhibited relatively lower accuracy, its LW-PLSR model still achieved an R^2 of 0.9473, with an RMSE of 0.0473 and an MAE of 0.0393. The prediction scatter plots of the single-modality models based on LIBS, HSI and SVI for sintered NiO/YSZ samples are

Table 1. Prediction performance of different models for nominal NiO mass fraction in sintered NiO/YSZ samples

Modality	Model	RMSE	MAE	R^2
LIBS	PLSR	0.0281 (0.0079)	0.0225 (0.0068)	0.9823 (0.0103)
	LW-PLSR	0.0244 (0.0078)	0.0204 (0.0062)	0.9854 (0.0109)
	K-ELM	0.0289 (0.0090)	0.0239 (0.0082)	0.9796 (0.0147)
	SVR	0.0276 (0.0086)	0.0222 (0.0072)	0.9814 (0.0137)
HSI	PLSR	0.0505 (0.0119)	0.0442 (0.0114)	0.9401 (0.0367)
	LW-PLSR	0.0450 (0.0129)	0.0387 (0.0101)	0.9488 (0.0424)
	K-ELM	0.0336 (0.0064)	0.0283 (0.0052)	0.9750 (0.0119)
	SVR	0.0339 (0.0048)	0.0285 (0.0035)	0.9738 (0.0142)
SVI	PLSR	0.0692 (0.0170)	0.0539 (0.0141)	0.8904 (0.0580)
	LW-PLSR	0.0473 (0.0075)	0.0393 (0.0081)	0.9473 (0.0361)
	K-ELM	0.0607 (0.0106)	0.0471 (0.0100)	0.9159 (0.0458)
	SVR	0.0621 (0.0110)	0.0468 (0.0095)	0.9114 (0.0510)

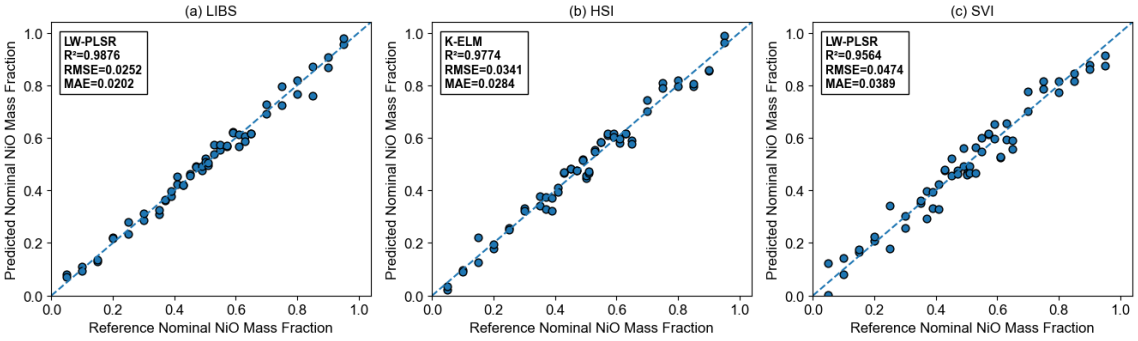

Fig. 4 Prediction scatter plots of the best-performing models for sintered NiO/YSZ samples based on (a) LIBS, (b) HSI and (c) SVI. For each modality, the model with the highest overall R^2 was selected for visualisation.

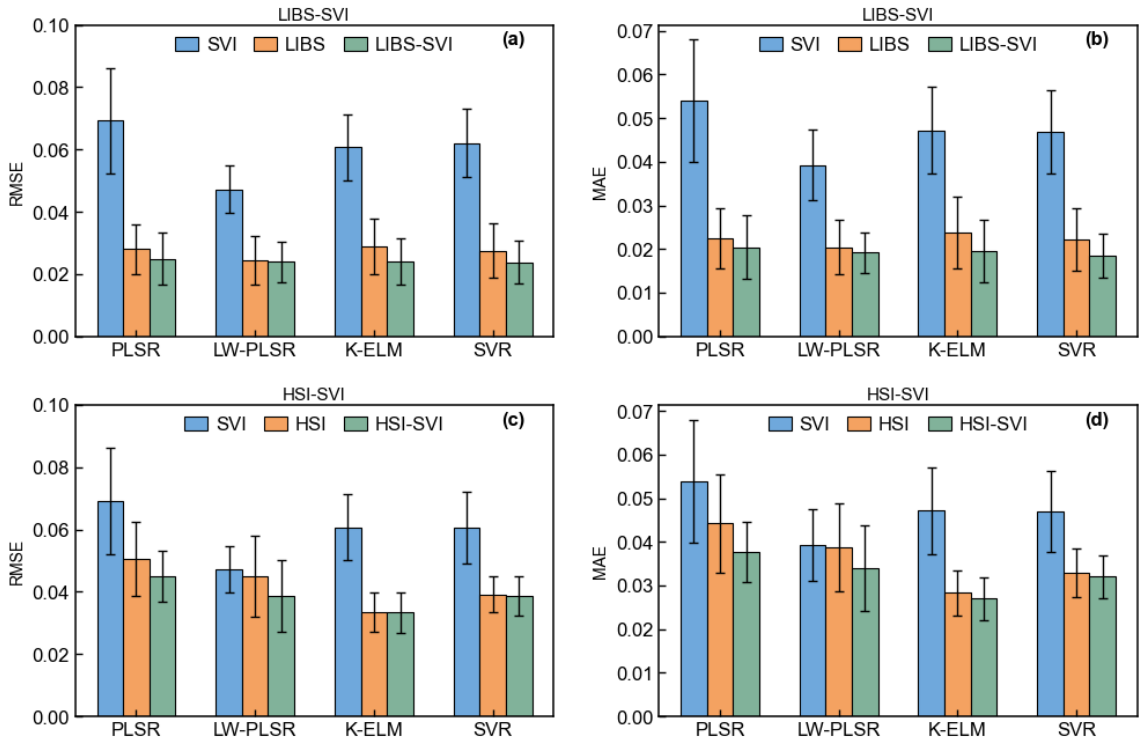

Fig. 5 Performance comparison of multimodal fusion models for sintered NiO/YSZ samples. (a, b) RMSE and MAE results of LIBS-SVI fusion. (c, d) RMSE and MAE results of HSI-SVI fusion.

Table 2. Prediction performance of different models for nominal NiO mass fraction for reduced Ni/YSZ samples.

Modality	Model	RMSE	MAE	R^2
LIBS	PLSR	0.0311 (0.0072)	0.0246 (0.0063)	0.9783 (0.0110)
	LW-PLSR	0.0273 (0.0066)	0.0216 (0.0047)	0.9817 (0.0141)
	K-ELM	**0.0235 (0.0093)**	**0.0200 (0.0081)**	**0.9860 (0.0116)**
	SVR	0.0256 (0.0091)	0.0210 (0.0075)	0.9844 (0.0114)
HSI	PLSR	0.0583 (0.0088)	0.0465 (0.0083)	0.9297 (0.0121)
	LW-PLSR	**0.0479 (0.0064)**	**0.0383 (0.0056)**	**0.9499 (0.0194)**
	K-ELM	0.0651 (0.0124)	0.0505 (0.0042)	0.9108 (0.0272)
	SVR	0.0621 (0.0154)	0.0461 (0.0087)	0.9169 (0.0352)
SVI	**PLSR**	**0.0753 (0.0179)**	**0.0595 (0.0107)**	**0.8676 (0.0827)**
	LW-PLSR	0.0858 (0.0343)	0.0663 (0.0219)	0.7902 (0.2277)
	K-ELM	0.0766 (0.0185)	0.0583 (0.0103)	0.8619 (0.0890)
	SVR	0.0836 (0.0182)	0.0660 (0.0104)	0.8424 (0.0809)

presented in Fig. S1. Fig. 4 shows the prediction scatter plots of the best-performing models for each modality, with the predicted values from all outer test folds and compared against the reference values to visualize prediction accuracy and agreement.

To further improve the quantitative prediction performance, decision-level multimodal fusion was performed by combining the prediction results from SVI with those from LIBS or HSI. The prediction scatter plots of the multimodal fusion models based on different modality combinations are provided in Supplementary Fig. S2. The fusion weight distributions for different modality combinations are provided in Table S1. Fig. 5 compares the prediction performance of the single-modality models and the corresponding fusion models, aiming to evaluate whether the additional information could further improve the prediction accuracy.

Overall, the multimodal fusion models generally improved the prediction performance compared with the SVI single-modality models. For LIBS-SVI fusion, the average RMSE across four regression algorithms was reduced by 58.5% relative to SVI and by 10.8% relative to LIBS. For HSI-SVI fusion, the average RMSE across four regression algorithms was reduced by 37.0% relative to SVI and by 5.9% relative to HSI. In general, the results demonstrate that decision-level multimodal fusion generally reduced prediction errors by integrating complementary information.

To further evaluate the statistical significance of the error reduction introduced by multimodal fusion, the Wilcoxon signed-rank test was performed on the composition-level paired absolute prediction errors of the fusion and single-modality models. The detailed results are provided in Table S2. The Wilcoxon test results indicate that multimodal fusion significantly reduced the prediction errors compared with SVI alone. In addition, further improvement over the primary modality was observed in some cases, suggesting that SVI provided complementary information for LIBS and HSI measurements.

Quantitative prediction of reduced Ni/YSZ samples. After evaluating the sintered NiO/YSZ samples, the same modelling strategy was applied to the reduced Ni/YSZ samples. Since the reduction process converts NiO into metallic Ni and may change the optical and spectral characteristics of the samples, it is necessary to further examine the prediction performance of LIBS, HSI and SVI.

Table 2 summarises the prediction performance of different modalities for reduced Ni/YSZ samples across five outer validation folds. Across all modality and algorithm combinations, R^2 ranged from 0.7902 to 0.9860, while RMSE and MAE ranged from 0.0235 to 0.0858 and from 0.0200 to 0.0663, respectively. LIBS remained the most accurate modality, with the K-ELM model achieving the highest R^2 of 0.9860 and the lowest RMSE and MAE of 0.0235 and 0.0200, respectively. For HSI, the optimal LW-PLSR model yielded an R^2 of 0.9499, an RMSE of 0.0479 and an MAE of 0.0383. The best SVI performance was also obtained using PLSR, with an R^2 of 0.8676, an RMSE of 0.0753 and an MAE of 0.0595. Compared with the sintered samples, the highest R^2 obtained by HSI decreased by 0.0251, while its RMSE and MAE increased by 0.0143 and 0.0100, respectively. For SVI, the highest R^2 decreased by 0.0797, accompanied by increases of 0.0280 in RMSE and 0.0202 in MAE. By contrast, the optimal LIBS model showed a slight increase of 0.0006 in R^2 and a decrease of 0.0009 in RMSE and 0.0004 in MAE after reduction, suggesting that its quantitative performance was less affected by the change in material state. The prediction scatter plots of the single-modality models based on LIBS, HSI and SVI for reduced Ni/YSZ samples are presented in Fig. S3. Fig. 6 shows the prediction scatter plots of the best-performing models for each modality in reduced Ni/YSZ samples, with the predicted values from all outer test folds and compared against the reference values to visualize prediction accuracy and agreement.

To further improve the quantitative prediction performance for reduced Ni/YSZ samples, decision-level multimodal fusion was also performed. The prediction scatter plots of the multimodal fusion models based on different modality combinations are

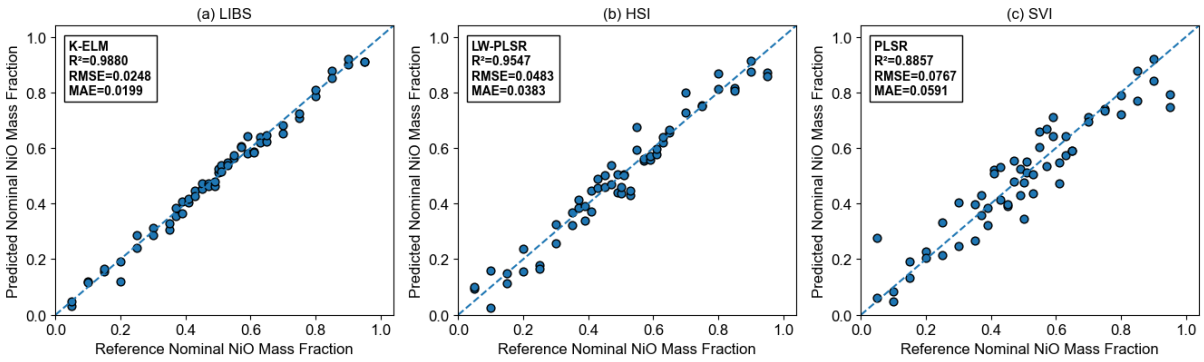

Fig. 6 Prediction scatter plots of the best-performing models for reduced Ni/YSZ samples based on (a) LIBS, (b) HSI and (c) SVI. For each modality, the model with the highest overall R^2 was selected for visualisation.

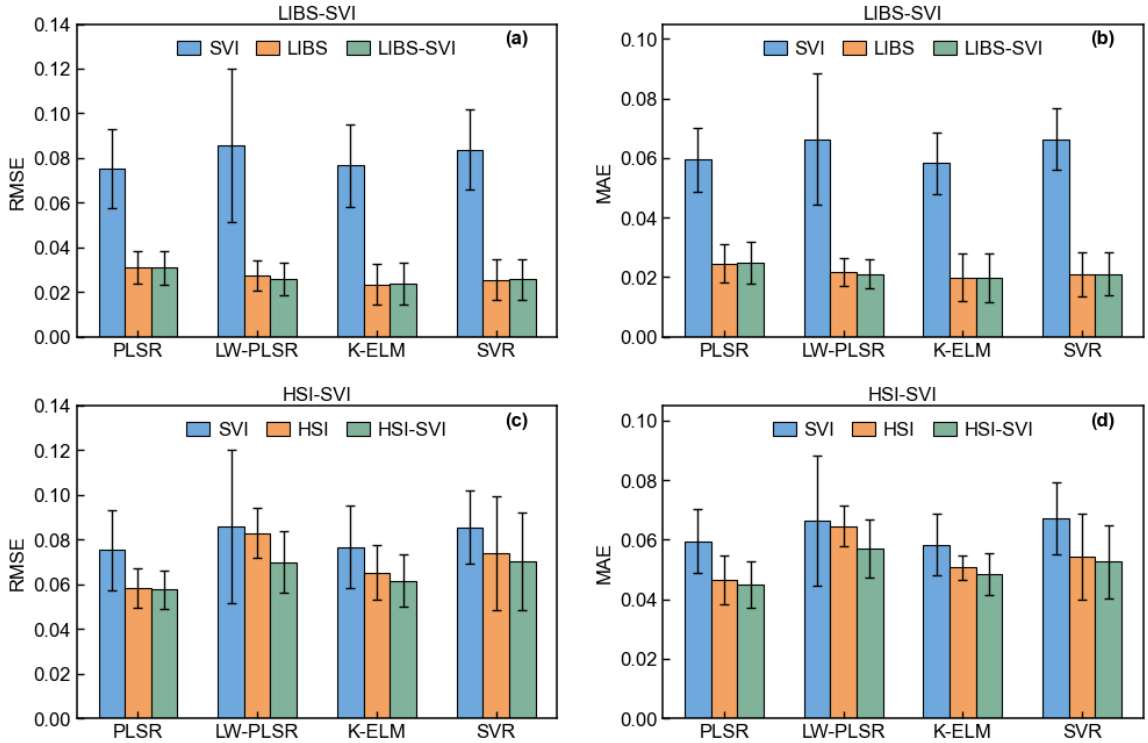

Fig. 7 Performance comparison of multimodal fusion models for reduced Ni/YSZ samples. (a, b) RMSE and MAE results of LIBS-SVI fusion. (c, d) RMSE and MAE results of HSI-SVI fusion.

provided in Fig. S4, and the corresponding fusion weight distributions are provided in Table S3. Fig. 7 compares the prediction performance of the single-modality models and the corresponding fusion models, aiming to evaluate whether the additional SVI information could further improve the prediction accuracy for nominal NiO mass fraction.

Overall, the multimodal fusion models improved the prediction performance compared with the SVI single-modality models for reduced Ni/YSZ samples. For LIBS-SVI fusion, the average RMSE across four regression algorithms was reduced by 66.5% relative to SVI and by 0.8% relative to LIBS. For HSI-SVI fusion, the average RMSE across four regression algorithms was reduced by 19.8% relative to SVI and by 7.7% relative to HSI. However, improvement over the primary modality depended on the regression model and was not observed in every case. SVI therefore provided useful complementary information in some, but not all, fusion models.

The same composition-level Wilcoxon signed-rank analysis

was performed for the reduced Ni/YSZ samples, with the detailed results provided in Table S4. The statistical significance of the error reduction depended on the fusion scheme and regression algorithm. LIBS-SVI fusion showed significant improvements over SVI across the evaluated regression models, whereas the significance of HSI-SVI fusion was model dependent. Compared with the primary modality, additional error reductions were observed in some cases, suggesting that SVI provided complementary information for LIBS- and HSI-based prediction.

Variable importance analysis. The VIP analysis revealed clear modality-dependent patterns in the variables contributing to composition prediction. For LIBS, the high VIP variables appeared as multiple discrete spectral features. The 228-232 nm region was predominantly associated with Ni emission lines, while the 337-346 nm region contained overlapping Ni and Zr features. Additional high VIP regions at longer wavelengths were more strongly associated with Zr emission, indicating that LIBS prediction relied on the combined variation of Ni-related emission and the Zr-containing YSZ fraction. For HSI, the most influential variables were mainly concentrated in the short-wavelength region. In NiO/YSZ, high VIP features were primarily distributed over approximately 342-450 nm, with a maximum contribution around 396 nm, whereas the reduced Ni/YSZ samples showed a shifted high-importance region approximately from 359 to 479 nm. For SVI, the importance distribution changed substantially after reduction. In NiO/YSZ, the G-channel showed the strongest overall contribution, with an averaged VIP of 1.0597 and 157 of 184 variables (85.3%) exhibiting mean VIP $>$ 1, compared with 88 (47.8%) and 93 (50.5%) variables in the R and B channels, respectively. After reduction to Ni/YSZ, the overall importance shifted toward the B channel, which showed the highest averaged VIP (1.0336) and 86 of 184 variables (46.7%) with mean VIP $>$ 1, whereas only 24 G-channel variables (13.0%) exceeded this threshold. The detailed VIP results are provided in Figs. S5 and S6. These distinct VIP distributions show that LIBS, HSI and SVI capture different aspects of composition-related information, supporting their complementary role in decision-level multimodal fusion.

Significance and implications. The results of this study demonstrate the feasibility of multimodal spectral methods for quantitative characterisation of SOFC electrode materials. LIBS, HSI and SVI provide different types of composition-related information. Among them, LIBS directly records element-specific emission signals and therefore shows strong quantitative capability for the prediction of specific chemical components. HSI provides reflectance spectra over multiple wavelengths, which can capture optical variations associated with material composition and surface characteristics. SVI records dynamic RGB responses under active illumination and extracts colour-change information from smartphone video signals. These different information sources indicate that the three modalities are not simply redundant, but can provide complementary information for composition prediction.

From a practical perspective, LIBS offers high prediction accuracy, but point-by-point measurement may limit its efficiency for large-area and high-throughput inspection. HSI and SVI can acquire optical information more rapidly, and SVI further has the advantages of low cost, simple hardware and good portability. However, compared with LIBS, optical sensing methods may extract less direct compositional information and can be more easily affected by surface morphology and optical conditions. Therefore, combining LIBS or HSI with SVI provides a useful strategy to balance analytical accuracy, measurement efficiency and system accessibility.

The multimodal fusion results show that adding SVI improved predictive performance in 14 of the 16 evaluated cases while introducing little additional measurement cost or system complexity. This represents the main practical advantage of the proposed fusion strategy. Rather than replacing LIBS or HSI, SVI serves as a supplementary modality that provides complementary optical information. In this framework, LIBS or HSI can provide accurate elemental or spectral information for model calibration, while smartphone-based SVI could support rapid screening and large-area evaluation of electrode samples.

The proposed framework may be applied to SOFC electrode fabrication and extended to the analysis after long-term operation. For example, SVI can first be used to rapidly screen large-area samples and identify possible composition variations or abnormal regions. LIBS or HSI measurements can then be selectively performed on representative locations for more accurate verification. This potential workflow can reduce the need for dense point-by-point measurements and improve the efficiency of material characterisation.

Nevertheless, this study was conducted using laboratory-prepared samples with controlled compositions. Real SOFC electrodes may show more complex microstructures, degradation behaviour and surface conditions.[29] For HSI, changes in surface morphology, porosity and illumination geometry may alter diffuse reflectance and scattering. For SVI, surface colour, illumination uniformity and imaging geometry may affect RGB responses. For LIBS, surface contamination, local component distribution and Ni/NiO conversion may influence plasma formation and emission intensity. Calibration models developed using homogeneous laboratory pellets therefore cannot be transferred directly to practical or aged electrodes without additional calibration and validation. In addition, the current dataset is still limited in sample diversity, which may affect the generalisation ability of conventional regression models. Therefore, this workflow remains to be validated using electrodes collected from more operating or aged SOFCs.

CONCLUSION

In this study, LIBS, HSI and SVI were combined with machine-learning regression for quantitative composition prediction of sintered NiO/YSZ and reduced Ni/YSZ anode samples. The three modalities provide complementary elemental, wavelength-resolved reflectance, and RGB-response information, respectively, which accounts for their different predictive behaviours and supports multimodal fusion. Decision-level weighted fusion was therefore performed for LIBS-SVI and HSI-SVI. By introducing complementary RGB information from SVI while retaining the dominant contribution of LIBS or HSI, the fusion models generally reduced prediction errors and, in several cases, improved the performance of the primary modality. Importantly, these improvements were achieved without substantially increasing measurement cost or operational complexity. The proposed framework therefore provides a practical and cost-effective approach for rapid quantitative evaluation and auxiliary quality control of SOFC anode materials.

ASSOCIATED CONTENT

The supporting information (Figs. S1−S6 and Tables S1−S4) is available at https://www.at-spectrosc.com

AUTHOR INFORMATION

Minfang Han received her PhD degree in 2002 from China University of Mining and Technology (Beijing). She is a professor in the Department of Energy and Power Engineering at Tsinghua University. Her research focuses on solid oxide fuel cells (SOFCs), solid oxide electrolysis cells (SOECs), advanced electrode materials, and hydrogen energy technologies. She has published more than 300 papers and holds over 180 invention patents. Her work mainly involves the development of high-performance solid oxide electrochemical devices and their applications in energy conversion and storage.

Zhe Wang received the PhD degree from The Pennsylvania State University, State College, PA, USA, in 2007. He is currently a Tenured Professor at Tsinghua University, Beijing, China, where he has worked since 2008. He has long-standing research experience in laser-induced plasma mechanisms, quantitative LIBS analysis, and coal-quality applications. He has published nearly 200 papers in LIBS and related fields, and been granted 37 invention patents. He has also contributed to LIBS-related national and industrial standards. His research interests include laser-induced breakdown spectroscopy, spectral imaging, and quantitative spectroscopic analysis.

Corresponding Authors

* M. F. Han

Email address: hanminfang@tsinghua.edu.cn

* Z. Wang

Email address: zhewang@tsinghua.edu.cn

Notes

The authors declare no competing financial interest.

ACKNOWLEDGMENTS

This research was supported by the National Key Research and Development Program of China (2023YFB4102900) and the Carbon Neutrality and Energy System Transformation (CNEST) Program initiated by Tsinghua University, and the National Natural Science Foundation of China (NSFC 52561160111).

REFERENCES

1. S. C. Singhal, *Solid State Ionics*, 2000, **135**, 305–313. https://doi.org/10.1016/S0167-2738(00)00452-5
2. B. Shri Prakash, S. Senthil Kumar, and S. T. Aruna, *Renew. Sustain. Energy Rev.*, 2014, **36**, 149–179. https://doi.org/10.1016/j.rser.2014.04.043
3. M. Brown, S. Primdahl, and M. B. Mogensen, *J. Electrochem. Soc.*, 2000, **147**, 475–485. https://doi.org/10.1149/1.1393220
4. N. Vivet, S. Chupin, E. Estrade, A. Richard, S. Bonnamy, D. Rochais, and E. Bruneton, *J. Power Sources*, 2011, **196**, 9989–9997. https://doi.org/10.1016/j.jpowsour.2011.07.010
5. D. Simwonis, F. Tietz, and D. Stöver, *Solid State Ionics*, 2000, **132**, 241–251. https://doi.org/10.1016/S0167-2738(00)00650-0
6. B. Song, E. Ruiz-Trejo, A. Bertei, and N. P. Brandon, *J. Power Sources*, 2018, **374**, 61–68. https://doi.org/10.1016/j.jpowsour.2017.11.024
7. T. Talebi, M. H. Sarrafi, M. Haji, B. Raissi, and A. Maghsoudipour, *Int. J. Hydrogen Energy*, 2010, **35**, 9440–9447. https://doi.org/10.1016/j.ijhydene.2010.04.156
8. S. Zarabi Golkhatmi, M. I. Asghar, and P. D. Lund, *Renew. Sustain. Energy Rev.*, 2022, **161**, 112339. https://doi.org/10.1016/j.rser.2022.112339
9. D. W. Hahn, and N. Omenetto, *Appl. Spectrosc.*, 2010, **64**, 335A–366A. https://doi.org/10.1366/000370210793561691
10. S. K. H. Shah, J. Iqbal, P. Ahmad, M. U. Khandaker, S. Haq, and M. Naeem, *Radiat. Phys. Chem.*, 2020, **170**, 108666. https://doi.org/10.1016/j.radphyschem.2019.108666

11. S. Imashuku, H. Taguchi, T. Kawamata, S. Fujieda, S. Kashiwakura, S. Suzuki, and K. Wagatsuma, *J. Power Sources*, 2018, **399**, 186–191. https://doi.org/10.1016/j.jpowsour.2018.07.088
12. P. Smyrek, T. Bergfeldt, H. J. Seifert, and W. Pfleging, *J. Mater. Chem. A*, 2019, **7**, 5656–5665. https://doi.org/10.1039/C8TA10328C
13. M. Kappeler, C. Basler, A. Brandenburg, D. Carl, and J. Wöllenstein, *Sensors*, 2022, **22**, 8816. https://doi.org/10.3390/s22228816
14. B. Liang, Q. Qing, J.-H. Luo, S. Liu, Z. Wang, J. Chen, and Y. Lu, *J. Anal. Test.*, 2026, **10**, 1–11. https://doi.org/10.1007/s41664-026-00470-6
15. O. Elmutasim, D. S. Dhawale, M. Pinczes, L. Hamid, S. Wong, S. Giddey, G. Paul, and S. Bhattacharya, *ACS Appl. Mater. Interfaces*, 2025, **17**, 65225–65241. https://doi.org/10.1021/acsami.5c12421
16. A. Bhargava, A. Sachdeva, K. Sharma, M. H. Alsharif, P. Uthansakul, and M. Uthansakul, *Heliyon*, 2024, **10**, e33208. https://doi.org/10.1016/j.heliyon.2024.e33208
17. J. Richter, S. Lorenz, A. Kaas, M. Fuchs, C. Röder, U. A. Peuker, J. Heitmann, and R. Gloaguen, *Metals*, 2024, **14**, 147. https://doi.org/10.3390/met14020147
18. S. Chouhan, B. Rasti, P. Ghamisi, S. Lorenz, M. C. Fuchs, and R. Gloaguen, *Proc. 12th Workshop on Hyperspectral Imaging and Signal Processing: Evolution in Remote Sensing (WHISPERS)*, 2022, 1–5. https://doi.org/10.1109/WHISPERS56178.2022.9955076
19. W. Song, H. Wang, and Y. H. Yun, *Food Chem.*, 2025, **462**, 140911. https://doi.org/10.1016/j.foodchem.2024.140911
20. W. Song, Z. Song, J. Vincent, H. Wang, and Z. Wang, *Talanta*, 2020, **216**, 120920. https://doi.org/10.1016/j.talanta.2020.120920
21. S. Yao, Z. Yu, Z. Hou, L. Guo, L. Zhang, H. Ding, Y. Lu, Q. Wang, and Z. Wang, *TrAC Trends Anal. Chem.*, 2024, **177**, 117795. https://doi.org/10.1016/j.trac.2024.117795
22. S. Zhao, Y. Zhao, Z. Hou, and Z. Wang, *Appl. Surf. Sci.*, 2023, **629**, 157415. https://doi.org/10.1016/j.apsusc.2023.157415
23. W. Song, G. Duan, L. An, W. Gu, Y. Lv, Z. Hou, H. Wang, and Z. Wang, *Sens. Actuators B Chem.*, 2026, **459**, 139880. https://doi.org/10.1016/j.snb.2026.139880
24. S. Wold, M. Sjöström, and L. Eriksson, *Chemom. Intell. Lab. Syst.*, 2001, **58**, 109–130. https://doi.org/10.1016/S0169-7439(01)00155-1
25. S. Kim, M. Kano, H. Nakagawa, and S. Hasebe, *Int. J. Pharm.*, 2011, **421**, 269–274. https://doi.org/10.1016/j.ijpharm.2011.10.007
26. G.-B. Huang, H. Zhou, X. Ding, and R. Zhang, *IEEE Trans. Syst. Man Cybern. Part B Cybern.*, 2012, **42**, 513–529. https://doi.org/10.1109/TSMCB.2011.2168604
27. A. J. Smola, and B. Schölkopf, *Stat. Comput.*, 2004, **14**, 199–222. https://doi.org/10.1023/B:STCO.0000035301.49549.88
28. W. Wang, D. Tran, and M. Feiszli, *Proc. IEEE/CVF Conf. Comput. Vis. Pattern Recogn. (CVPR)*, 2020, 12692–12702. https://doi.org/10.1109/CVPR42600.2020.01271
29. M. S. Khan, S. B. Lee, R. H. Song, J. W. Lee, T. H. Lim, and S. J. Park, *Ceram. Int.*, 2016, **42**, 35–48. https://doi.org/10.1016/j.ceramint.2015.09.006